Observations of creep of polar firn at different temperatures

Yuan Li[1,3], Kaitlin Keegan[2], Ian Baker[1]

[1]Thayer School of Engineering, Dartmouth College, Hanover, NH, 03755, USA

[2]Department of Geological Sciences & Engineering, University of Nevada, Reno, Reno, NV, 89557, USA

[3]X-Here (Future ice-based Hydrogen energy & resilient environments) Trek Laboratory (Establishing), Howard Beach, NY, 11414, USA

Correspondence to: Ian Baker (ian.baker@dartmouth.edu)

Abstract

To improve our understanding of firn compaction and deformation processes, constant-load compressive creep tests were performed on specimens from a Summit, Greenland (72°35' N, 38°25' W) firn core that was extracted in June, 2017. Cylindrical specimens were tested at temperatures of –5°C, –18°C and –30°C from depths of 20 m, 40 m and 60 m at stresses of 0.21 MPa, 0.32 MPa and 0.43MPa, respectively. The microstructures were characterized before and after creep using both X-ray micro-computed tomography (micro-CT) and thin sections viewed between optical crossed polarizers. The results of these experiments comprise a novel data set on the creep of firn at three depths of a firn column at three different temperatures, providing useful calibration data for firn model development. Examining the resulting strain vs. time and strain vs. strain rate curves from the creep tests revealed the following notable features. First, the time exponent k was found to be 0.34–0.69 during transient creep, which is greater than the 0.33 usually observed in fully-dense ice. Second, the strain rate minimum (SRmin) in secondary creep occurred at a greater strain from specimens with lower density and at higher temperatures. Third, tertiary creep occurred more easily for the lower-density specimens at greater effective stresses and higher temperatures, where strain softening is primarily due to recrystallization. Fourth, the SRmin is a function of the temperature for a given firn density. Lastly, we developed empirical equations for inferring the SRmin, as it is difficult to measure during creep at low temperatures. The creep behaviors of polar firn, being essentially different from full-density ice, imply that firn densification is an indispensable process within the snow-to-ice transition, particularly firn deformation at different temperatures connected to a changing climate.

Keywords: Firn; Creep; Activation energy; Microstructure; Temperature

1. Introduction

Understanding firn compaction and densification experimentally is critical for developing physics-based firn models that are necessary for many glaciological applications, e.g. reconstructing ice-core paleoclimate records, interpreting ice-mass changes from satellite altimetry data, and even developing clean hydrogen production and storage technology (Li, 2023a; 2024a; 2024b; 2024c). However, the firn models used for these applications are empirical and are known to perform poorly outside of their calibration range (Lundin et al., 2017). Thus, a better understanding of firn compaction is necessary to refine firn models for these important glaciological applications. Laboratory compressive experiments on firn and ice improve our understanding of their respective flow laws and advance the development of firn models under a range of conditions. Numerous studies of firn and ice deformation have been conducted (e.g. Steinemann, 1954; Glen, 1955; Landauer, 1958; Mellor, 1975; Salm, 1982; Maeno and Ebinuma, 1983; Jacka, 1984; Ambach and Eisner, 1985; Budd and Jacka, 1989; Li et al., 1996; Meussen et al., 1999; Petrenko and Whitworth, 1999; Bartelt and von Moos, 2000; Jacka and Li, 2000; Durham et al., 2001; Goldsby and Kohlstedt, 2001; Hooke, 2005; Song et al., 2006a, 2006b, 2008; Theile et al., 2011; Treverrow et al., 2012; Hammonds and Baker, 2016, 2018; Li and Baker, 2021, 2022a), but there are few reports about their mechanical behaviors at different temperatures. Temperature is a key component of firn and ice-flow models, as the deformation of firn, polythermal glaciers, and temperate glaciers is significantly influenced by the temperature.

Notably, the mechanical behavior of two-phase flow coupling the airflow with the ice matrix deformation has not yet been performed experimentally hitherto, even though the role of the

55 microstructures of firn on airflow has been studied (Albert et al., 2000; Courville et al., 2010;
56 Adolph and Albert, 2014). This difficulty is largely due to the limitations of the observation
57 techniques of nondestructive visualization of the microstructures during snow and firn
58 deformation. Thus, caution should be taken when extending the conclusions to ice sheet and
59 glacier scales from sample laboratory experiments. Macroscopically, the creep of firn obeys a
60 power-law dependence of the strain rate on the stress at constant stresses and temperature, similar
61 to that of full-density ice (Li and Baker, 2022a). Note that both the diffusivity and permeability of
62 the air in the pores (Albert et al., 2000; Courville et al., 2010; Adolph and Albert, 2014) impact
63 heat conduction of the ice matrix, and hence the grain growth. This is tightly tied to the
64 micro-mechanisms, e.g. grain-boundary and lattice diffusion of the ice crystals (Li and Baker,
65 2021), superplastic deformation and inter-particle sliding from dislocation motion in the ice necks
66 (Bartelt and Von Moos, 2000), and likely rearrangement of the ice particles (Perutz and Seligman,
67 1939; Anderson and Benson, 1963; Ebinuma and Maeno, 1987).
68
69 Through experiments on isotropic ice samples subjected to uni-axial compaction at octahedral
70 stresses of 0.1–0.8 MPa and temperatures from –45ºC to –5ºC, Jacka and Li (2000) determined
71 the mechanisms involved in the empirical *power-law flow*, which was derived by Glen (1955) for
72 stresses ranging from 0.1–1 MPa at temperatures spanning from –13ºC to the melting-point. They
73 found that dynamic recrystallization predominated at higher temperatures and stresses, whereas
74 crystal rotation governed at lower temperatures and stresses. Later, Goldsby and Kohstedt (2001)
75 found that ice could exhibit *superplastic flow*, which depends inversely on the grain size,
76 particularly for fine-grained ice, while both dislocation creep and basal slip-limited creep were

unrelated to the grain size at stresses of 0.1 MPa or less over a wide range of temperatures. Moreover, Baker and Gerberich (1979) reported that the apparent activation energy for creep for polycrystalline ice, which was derived from tests at constant stress and temperatures ranging from –40°C to –5°C, increased with increasing volume fraction of inclusions (bubbles, impurities, dust, and air clathrate hydrates). Such inclusions governed the evolution of grain size related to thermal activations. The activation energies for the creep of snow and ice have been determined by a number of authors, and values ranging from 58.6–113 kJ mol^{-1} were obtained under both uniaxial and hydrostatic experiments for snow with a density of ~400 kg m^{-3} at –13.6°C to –3.6°C (Landauer, 1958); 44.8–74.5 kJ mol^{-1} from snow with densities of 440–830 kg m^{-3} at –34.5°C to –0.5°C (Mellor and Smith, 1966); ~72.9 kJ mol^{-1} for firn with a density of 320–650 kg m^{-3} at the South Pole (Gow, 1969); 69 ± 5 kJ mol^{-1} for a mean snow density of 423 ± 8 kg m^{-3} at –19°C to –11°C (Scapozza and Bartelt, 2003); the 78 kJ mol^{-1} from polycrystalline ice compression deformation at a temperature of –10 °C (Duval and Ashby, 1983); ~60 kJ mol^{-1} for artificial and natural ice at the South Pole (Pimienta and Duval, 1987); and 78 ± 4 kJ mol^{-1} for monocrystal ice at –20°C to –4.5°C and 75 ± 2 kJ mol^{-1} for bicrystal ice at –15°C to –4.5°C (Homer and Glen, 1978). In summary, the flow law of polycrystalline ice and firn depends on the effects of recrystallization, grain size, inclusions (Mellor and Testa, 1969; Vickers and Greenfield, 1968; Barnes et al., 1971; Baker and Gerberich, 1979; Goodman et al., 1981), and the temperature.

With advanced observation techniques, the relevant microstructural parameters of snow and firn have been characterized by a number of scientists (Arnaud et al., 1998; Coleou et al., 2001; Flin et al., 2004; Wang and Baker, 2013; Wiese and Schneebeli, 2017; Li, 2022). Using X-ray

micro-computed tomography (micro-CT), Li and Baker (2022b) characterized metamorphism from snow to depth hoar under opposing temperature gradients. Only rarely has work been performed on the co-effects of temperature and stress on the densification of firn while simultaneously visualizing the microstructural changes using a micro-CT. For example, Schleef et al. (2014) reported that densification under varying conditions of overburden stress and temperature from natural and laboratory-grown new snow showed a linear relationship between density and the specific surface area (SSA). To this end, the aim of our present work is to investigate the temperature dependence of the creep of polar firn and relate this to the change of microstructure determined using micro-CT studies on firn obtained from Summit, Greenland in 2017. As is well known, temperature is a key parameter affecting the flow of firn and ice, and plays a determined role in their deformation, especially for polythermal and temperate glaciers. Due to the great difficulty of analyzing firn and ice deformation with the presence of liquid water, this work focuses on the firn creep from the dry snow zone, i.e., areas without meltwater, at different temperatures.

2. Samples and measurements

2.1 *Samples*

Three cylindrical samples (22 ± 0.5 mm diameter; 50 ± 0.5 mm high) were produced at each of three depths of 20 m, 40 m and 60 m from the same 2017 Summit, Greenland firn core that was studied in Li and Baker (2022a). Both the densities and porosities of these above samples are typical of values in the snow-to-ice transition zone as introduced in Section 1. It is important to note that the reduction in effective stress with increasing depth is evident in samples taken from

these three specified depths (**Appendix A**). Before creep testing, one cylindrical firn samples from each depth was stored at a temperature of –5 ± 0.5°C, –18 ± 0.5°C, and –30 ± 0.5°C for two days to achieve thermal equilibrium (Li and Baker, 2022a). It's also important to note that firn is a heterogeneous material that can have variations in layering, fabric, grain size, and impurity concentration across short distances. Thus, care was taken to extract the three replicate samples from the core at each depth as closely as possible to reduce the variability in their initial conditions.

2.2 Creep measurements

Three home-built creep jigs were placed in individual Styrofoam boxes in three different cold rooms that were held at temperatures of –5 ± 0.5°C, –18 ± 0.5°C and –30 ± 0.5°C. Each creep jig consists of an aluminum base plate and three polished aluminum-guide rails passing through linear bearings that hold the upper aluminum loading plate (**Figure 1**). A linear voltage differential transducer (LVDT-Omega LD-320: resolution of 0.025%; linearity error of ± 0.15% of full-scale output), parallel to the three aluminum-guide rails, was located adjacent to the center of the upper plate, and fixed firmly using a screw through the plate (**Figure 1**) for measuring the displacement during a test. The displacement was logged every 5 seconds using a Grant SQ2010 datalogger (accuracy of 0.1%). Temperatures were logged at 300-second time intervals over the entire test period, using a k-type thermocouple (Omega RDXL4SD thermistor: resolution of 0.1°C) that was mounted inside each box. In this work, specimens were tested at temperatures of –5 ± 0.2°C, –18 ± 0.2°C and –30 ± 0.2°C from depths of 20 m (applied stress 0.21 MPa), 40 m (0.32 MPa) and 60 m (0.43 MPa). There are smaller error bars for the temperature of the specimens

than the room temperature because the creep jigs were in insulated Styrofoam boxes. The stresses were chosen based on experience from previous tests (Li and Baker, 2022a) in order to give measurable creep rates in a reasonable time.

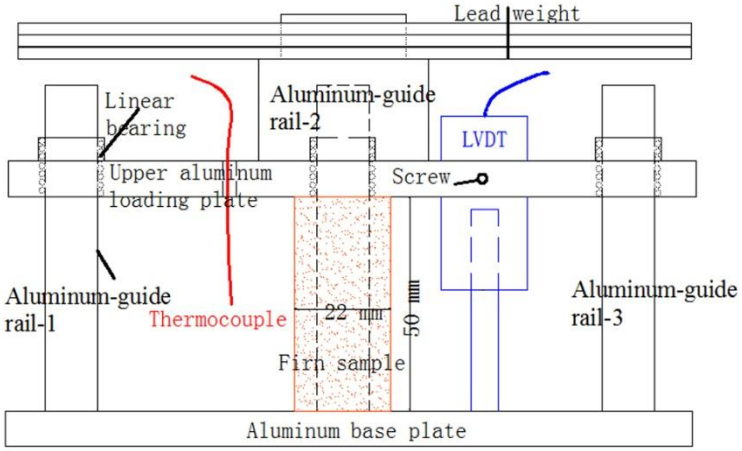

Figure 1: Schematic illustrating the home-built compressive creep jigs. More details can be found in (Li & Baker, 2022a).

2.3 *X-ray micro-computed tomography (micro-CT)*

Each specimen at each depth and temperature combination was scanned using a Skyscan 1172 micro-CT, before and after creep testing. Each micro-CT scan lasted ~2 h. The cubic Volume of Interest (VOI, a side length of 8 mm) was taken from near the center of the firn specimen as conducted in Li and Baker (2022a). The microstructural parameters obtained from the micro-CT data are the SSA, the mean structure thickness of the ice matrix (S.Th), the area-equivalent circle diameter of the pores (ECDa), the total porosity (TP), the closed porosity (CP), and the structure model index (SMI). The SSA (mm^{-1}) is the ratio of the ice surface area to total firn volume (ice

plus air) in a VOI analytical element, and is calculated using the hexahedral marching cubes algorithm via CTAn software (Wang and Baker, 2013). It characterizes the thickness and complexity of the firn microstructure. Changes in SSA indicate a change in free energy of the ice surfaces, the decrease of which represents the occurrence of sintering-pressure. The S.Th (mm) is the mean structure thickness of an ice matrix (Hildebrand and Ruegsegger, 1997), which represents the characteristic size of an ice particle in the firn, where the ice particle consists of one or many crystals or grains. It is measured based on the largest sphere diameter that encloses a point in the ice matrix and is completely bounded within solid surfaces. The ECDa (mm) is the diameter of a circle having the same area as the average for all pores in the VOI from the 2-D binary images, indicative of the characteristic size for the void space (Adolph and Albert, 2014). The TP (%) is the ratio of the pore volume, including both open and closed pores, to the total VOI. The CP (%) is the ratio of the volume of the closed pores to the total volume of solid plus closed pores volume in a VOI, while the open porosity (%) is the ratio of the volume of the open pores to the total VOI. The SMI is calculated based on the dilation of a 3-D voxel model (Hildebrand and Ruegsegger, 1997) $\mathrm{SMI} = 6\left(S' \times V\right)/S^2$, where S' is the change in the surface area due to dilation, and V and S are the object volume and surface area, respectively. It indicates the prevalent ice curvature, negative values of which represent a concave surface, e.g. the hollow air structure surrounded by an ice matrix. The more negative the SMI value, the more spherical the pore. Notably, the micro-CT-derived density of each specimen agrees well with the bulk density measured using the mass-volume approach (Li and Baker, 2021).

2.4 Thin section preparation and imaging

Thin sections for optical photographs before and after creep testing were cut from bulk specimens, one side of which was first smoothed with a microtome. This side was then frozen onto a glass plate (100 × 60 × 2 mm) by dropping supercooled gas-free water along its edges. Its thickness was reduced to ~2 mm by a band saw, and finally thinned further to a uniform thickness of ~0.5 mm using a microtome. Images were captured using a digital camera after each thin section was placed on a light table between a pair of crossed polarizing sheets.

3 Results and discussion

3.1 *Microstructures before creep*

Increasing firn density with increasing depth from either of the –5°C, –18°C, and –30°C specimens can be readily recognized by visual inspection of the micro-CT 3-D reconstructions of the firn microstructure (**Figure 2**). Correspondingly, the microstructural parameters, with the exception of the CP, changed monotonically with increasing depth at each temperature, e.g. the –30°C samples increased in density from 591 ± 1.4 kg m^{-3}, to 683 ± 4.2 kg m^{-3}, to 782 ± 1.5 kg m^{-3}, decreased in SSA from 4.64 ± 0.04 mm^{-1}, to 3.3 ± 0.06 mm^{-1}, to 2.39 ± 0.01 mm^{-1}, and decreased in TP from 35.6 ± 0.05%, 25.6 ± 0.4%, to 14.8 ± 0.2% at 20, 40, and 60 m, respectively (**Table 1)**. These above changes are similar to those previously observed in this firn core (Li and Baker, 2022a), implying that the sintering-pressure mechanism plays a crucial role in the densification of polar firn due to the increasing overburden of snow and firn with increasing depth. However, the microstructures of the samples from the three temperatures at each depth show little variability and do not monotonically change with temperature, e.g. at 20 m depth the –5°C, –18°C, and –30°C samples having densities of 589 ± 1.3 kg m^{-3}, 615 ± 2.5 kg m^{-3}, and 591 ± 1.4 kg m^{-3}, and

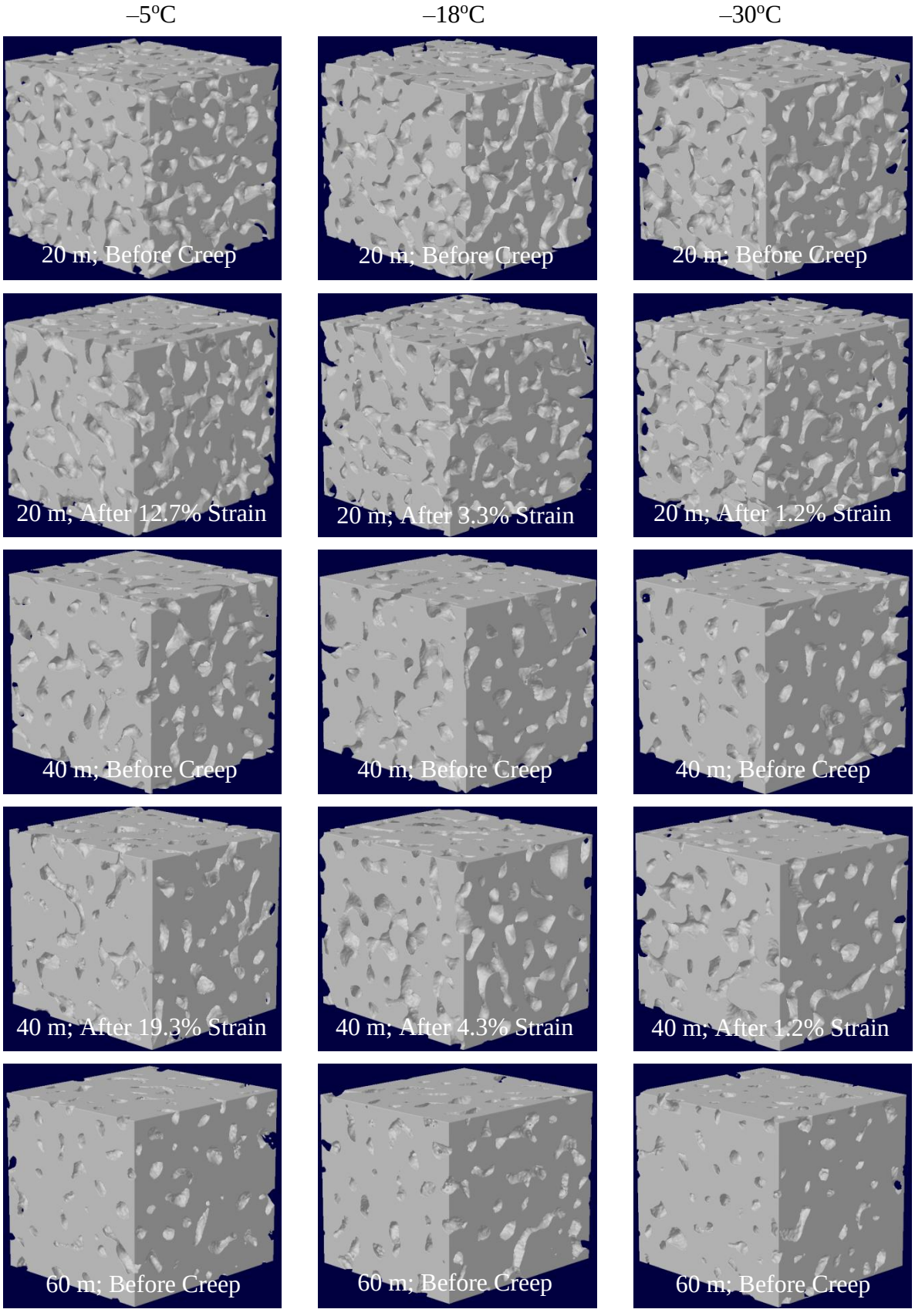
–5°C
–18°C
–30°C
20 m; Before Creep
20 m; Before Creep
20 m; Before Creep
20 m; After 12.7% Strain
20 m; After 3.3% Strain
20 m; After 1.2% Strain
40 m; Before Creep
40 m; Before Creep
40 m; Before Creep
40 m; After 19.3% Strain
40 m; After 4.3% Strain
40 m; After 1.2% Strain
60 m; Before Creep
60 m; Before Creep
60 m; Before Creep

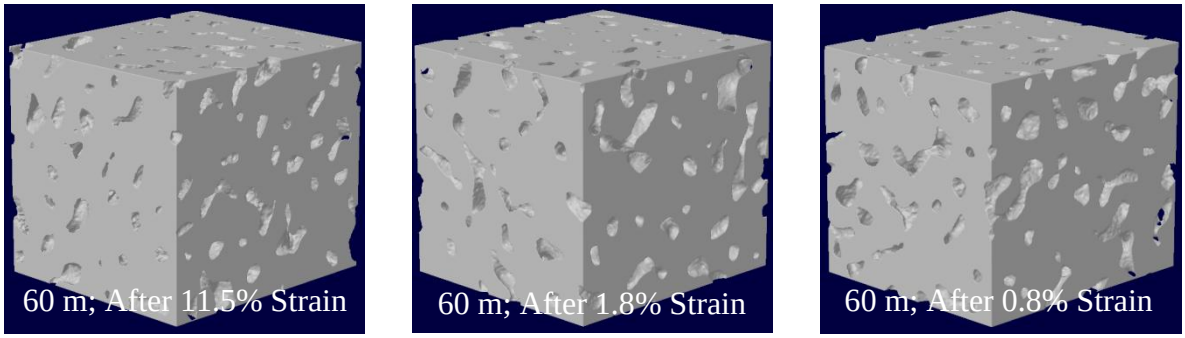

Figure 2: Micro-CT 3-D reconstructions (the side length of each cubic volume of interest is 8 mm) of specimens before and after creep testing at the depths and temperatures shown. Grey voxels represent ice in the firn structure.

Table 1. Microstructural parameters derived from Micro-CT for samples at –5°C, –18°C, and –30°C from depths of 20 m, 40 m, and 60 m before creep.

20m							
T °C	Density kg m^{-3}	SSA mm^{-1}	S.Th mm	TP %	CP %	SMI	ECDa mm
–5	589±1.3	4.74±0.03	0.732±0.001	35.9±0.08	0.03±0.002	-0.31±0.04	1.07±0.005
–18	615±2.5	4.51±0.04	0.758±0.001	33.1±0.2	0.01±0.001	-0.57±0.01	0.995±0.013
–30	591±1.4	4.64±0.04	0.747±0.004	35.6±0.05	0.02±0.001	-0.27±0.05	1.09±0.004

40m							
T °C	Density kg m^{-3}	SSA mm^{-1}	S.Th mm	TP %	CP %	SMI	ECDa mm
–5	685±1.4	3.26±0.04	0.95±0.004	25.5±0.1	0.015±0.001	-1.85±0.11	0.857 ±0.005
–18	669±0.6	3.41±0.04	0.914±0.003	27.1±0.03	0.01±0.001	-1.69±0.09	0.892±0.002
–30	683±4.2	3.30±0.06	0.94±0.01	25.6±0.4	0.021±0.005	-1.87±0.13	0.86±0.01

60m							
T °C	Density kg m^{-3}	SSA mm^{-1}	S.Th mm	TP %	CP %	SMI	ECDa mm
–5	790±1.0	2.34±0.03	1.1±0.003	14.0±0.1	0.11±0.01	-4.81±0.22	0.594±0.003
–18	780±0.5	2.37±0.03	1.08±0.01	15.2±0.06	0.014±0.007	-4.8±0.2	0.632±0.001
–30	782±1.5	2.39±0.01	1.076±0.0003	14.8±0.2	0.02±0.001	-4.92±0.14	0.639±0.002

Note: SSA is the specific surface area, S.Th is the structure thickness, TP is the total porosity, CP

is the closed porosity, SMI is the structure model index, and ECDa is the area-equivalent circle diameter.

SSAs of 4.74 ± 0.03 mm^{-1}, 4.51 ± 0.04 mm^{-1}, and 4.64 ± 0.04 mm^{-1}, respectively (**Figures 2–3**; **Table 1)**. Here, despite the –18°C specimen having a higher density than the two others at –5°C and –30°C, is not possible to conclude that the sintering of firn is not directly related to the temperature. This is likely because a thermal equilibration period of two days in the absence of compression is too short to sufficiently exert the influence of temperature on firn sintering. The microstructural differences seen in these specimens more likely arose from the initial samples themselves, which were anisotropic and heterogeneous even if taken from the same depth, attributed to firn pre-deformation and partial annealing before experiments (Li and Baker, 2022a).

3.2 *Microstructures after creep*

The microstructural evolution is characterized by the microstructural parameters shown in **Figure 3**. The largest changes occurred in the –5°C specimens due to the higher temperature, i.e., the density, S.Th, and CP increased, while the ECDa, TP, SSA, and SMI decreased, indicative of consolidation of the firn after creep. It is important to note that for the 60 m sample tested at –5°C, there was no change in density, i.e., 790.2 ± 1 kg m^{-3} before creep vs. 790.7 ± 0.9 kg m^{-3} after creep, or TP, i.e., 14.0 ± 0.1% before creep vs. 13.9 ± 0.1% after creep. This lack of microstructural change is due to the high initial density, which was close to the firn pore close-off density of ~830 kg m^{-3}. Thus, the creep of this sample may involve a transition from firn to

bubbly ice, as is also indicated by the increase in CP, which would have made it difficult to compress further. Intriguingly, some of the changes in microstructure observed in the micro-CT 3-D reconstructions from the specimens before and after creep, e.g. the distribution of ice-space, are indistinguishable in **Figure 2**. This is presumably due to the relatively large initial particle size, or from radial dilation exceeding the axial compression because of the small strains that occurred at relatively low temperatures.

One exception to the expected microstructural change after creep was the decrease of CP, which was likely due to the measurement uncertainty of the micro-CT (Burr et al., 2018), or radial expansion of the specimen during creep. Another exception was the decrease in density after creep for the –18°C specimen at 20 m and the –30°C specimen at 60 m, which arose due to a de-densification effect produced by temperature gradient metamorphism, as confirmed by the increase of both TP and S.Th (Li and Baker, 2022b). The thermal gradient appears to be associated with a fluctuation of 0.2°C around the test temperature, similar to temperature cycling occurred within firn (Mellor and Testa, 1969; Weertman, 1985), which stems from the thermometer's inherent accuracy as noted in Section 2.2 (–5 ± 0.2°C, –18 ± 0.2°C and –30 ± 0.2°C). In the relatively simple deformation found at ice-sheet dome sites, such as Summit, there is no mechanism to decrease density during compression. At sites closer to the ice sheet margins, cracking due to extension of the ice may cause a localized decrease in density. The rate of firn densification should decrease with increasing depth at a given temperature, due to the decrease of effective stress with increasing depth (**Appendix A**). As a matter of fact, the density of the –5°C samples after creep increased by 32 kg m^{-3}, 44 kg m^{-3}, and 0.5 kg m^{-3} for the 20 m, 40

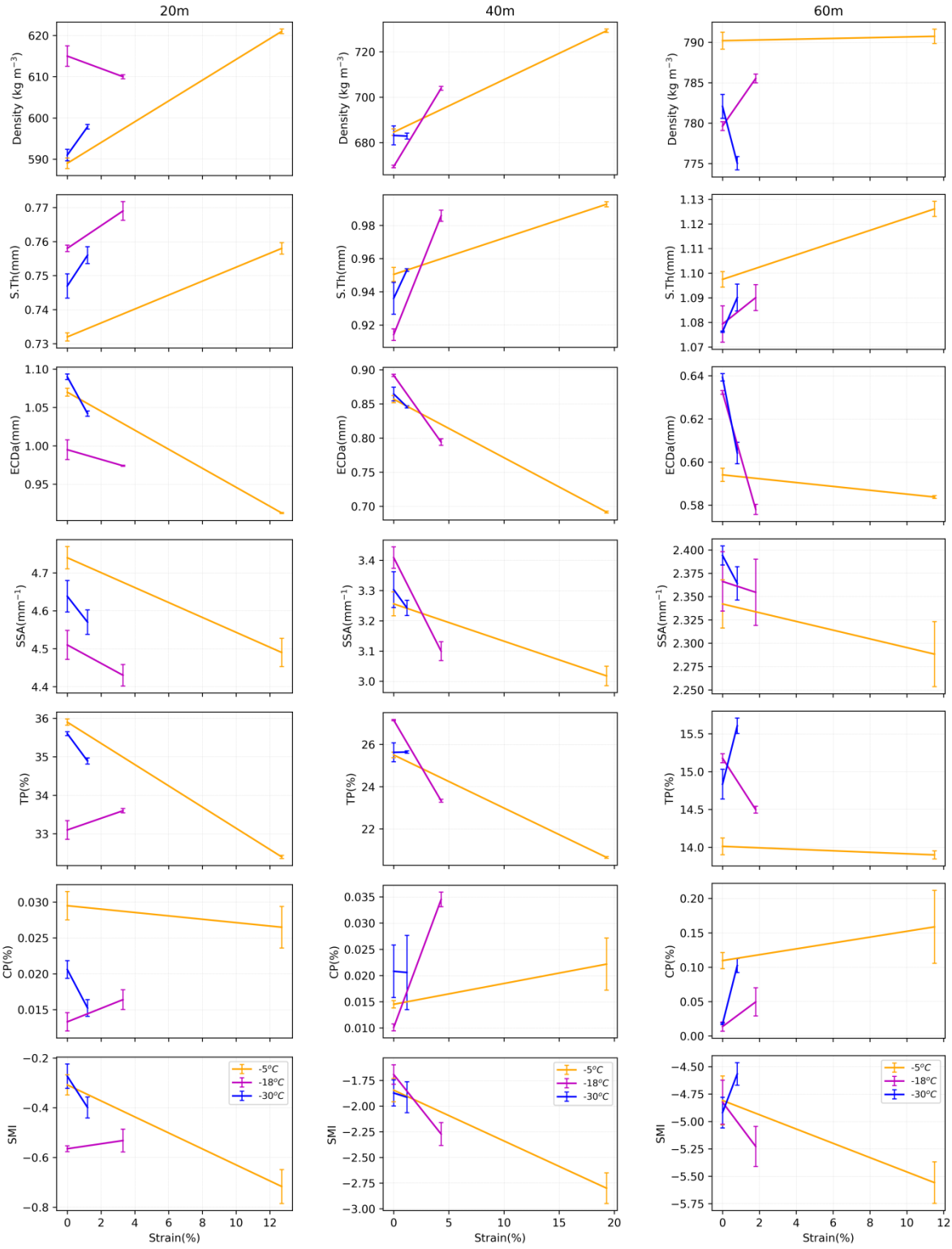

Figure 3: Density, structure thickness (S.Th), area-equivalent circle diameter (ECDa), specific surface area (SSA), total porosity (TP), closed porosity (CP), and structure model index (SMI) of the firn samples before and after creep at three temperatures (orange, magenta, and blue lines)

from depths of 20 m, 40 m and 60 m. Error bars indicate the variation of each microstructural parameter as derived from three different VOIs of the same sample.

m, and 60 m samples, respectively. The 44 kg m^{-3} unexpectedly outnumbers the 32 kg m^{-3}, implying that the densification of firn is also affected by other undetermined factors, e.g. the effect of inclusions, in addition to the stress and temperature.

Another way to investigate microstructure changes before and after creep tests is to compare their grain sizes using thin sections. As an example, **Figure 4** shows optical micrographs of thin sections made from the –5ºC sample at 40 m before and after creep to a strain of 19.3%, where the significant reduction in grain size from 0.8 ± 0.67 mm to 0.5 ± 0.32 mm implies the occurrence of recrystallization during testing. However, it is also unclear at what strain recrystallization

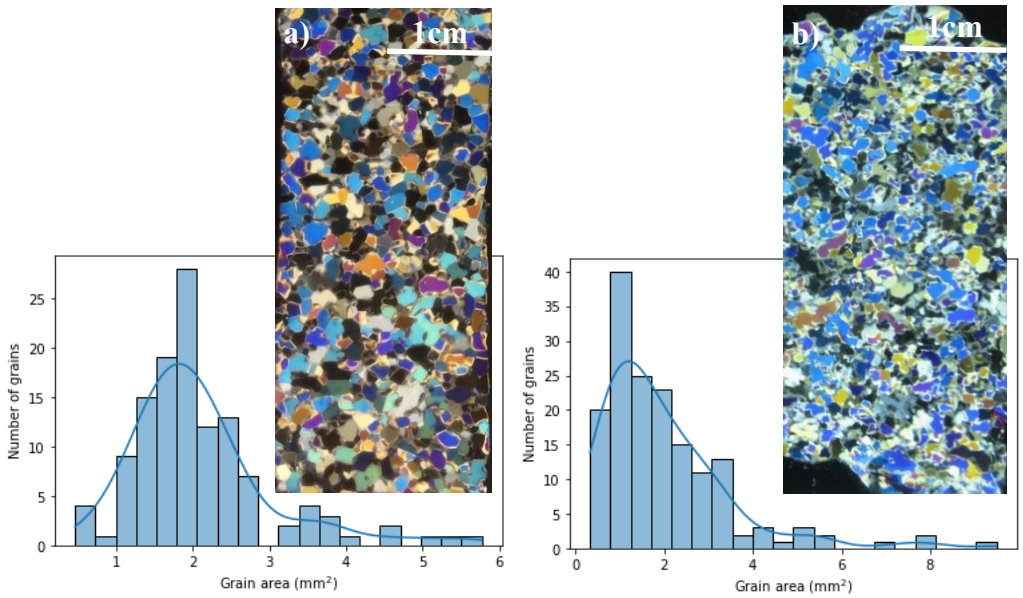

Figure 4: Optical micrographs of thin sections, and the distribution of grain sizes for the 40 m sample at –5°C (a) before and (b) after creep (19.3% strain).

was initiated in each test, as noted in Li and Baker (2022a). Recrystallization occurs frequently at a temperature higher than the homologous temperatures of 0.9 T_m. However, no evidence was found for recrystallization after testing at the relatively cold –18°C and –30°C conditions, probably due to the small creep strains at these relatively low temperatures. The creep mechanisms for these samples, and whether the mechanisms were different at different temperatures, could not be determined from the micro-CT-derived microstructural observations alone, because the micro-CT can only capture the microstructure before and after creep. Instead, plots of both strain vs. time and strain rate vs. strain can be used to elucidate the onset of recrystallization during creep (Sections 3.3 and 3.4; Ogunmolasuyi, et al., 2023).

3.3 *Relationship between strain and time*

Figure 5 shows the strain vs. time creep curves. The specimens at –5°C at 20 m and –18°C at 20 m, 40 m, and 60 m, show decelerating transient creep and quasi-viscous steady-state creep, while the specimens at –5°C at 40 m and 60 m show transient, secondary, and accelerating tertiary creep. Note that the curves from the –30°C specimens are not easily interpreted due to a large amount of noise arising from both the insufficient resolution of a linear voltage differential transducer (Li and Baker, 2022a) and the very small strains. The transient creep stage may be caused by strain hardening that occurs from the yield point to the ultimate strength (Glen, 1955; Jacka, 1984). The

plastic deformation is accommodated by an increase in dislocation density through dislocation multiplication or the formation of new dislocations (Frost and Ashby, 1982; Duval et al., 1983; Ashby and Duval, 1985), which leads to an increase of the firn strength as the dislocations become pinned or tangled, and thus more difficult to move. The initial decrease of creep rate may also be related to the rearrangement of dislocations into a more stable pattern through a dragging mechanism (Weertman, 1983) for the –5°C specimens. The tertiary creep stage may be associated with strain softening deriving either from the thermally-activated processes at the high homologous temperature approaching the melting point of ice, or from recrystallization (Li and Baker, 2022a). Clearly, the creep rate of firn is sensitive to temperature under constant stress at a given depth, *viz.*, the creep rate increases with increasing temperature (**Figure 5**). Incidentally, there is no evidence of the onset of recrystallization in the creep curves themselves despite the thin-section observation that –5°C specimens clearly underwent recrystallization during creep (Section 3.2).

A modified Andrade-like equation $\varepsilon = \beta t^k + \varepsilon_0$ in Li and Baker (2022a) was used to describe the transient creep behavior of the firn, in which the primary creep was well represented in black dashed lines on the creep curves in **Figure 5**. The time exponent *k*, derived from the above equation, ranges from 0.34–0.69: the data for the –30°C specimens are excluded since the noise in the results makes them uninterpretable. These *k* values are also smaller than those from monocrystalline and bicrystalline ice: 1.9 ± 0.5, 1.5 ± 0.2, and 1.3 ± 0.4 (Li and Baker, 2022a and references therein). We also note that the *k* values from the specimens at –5°C from 20–60 m

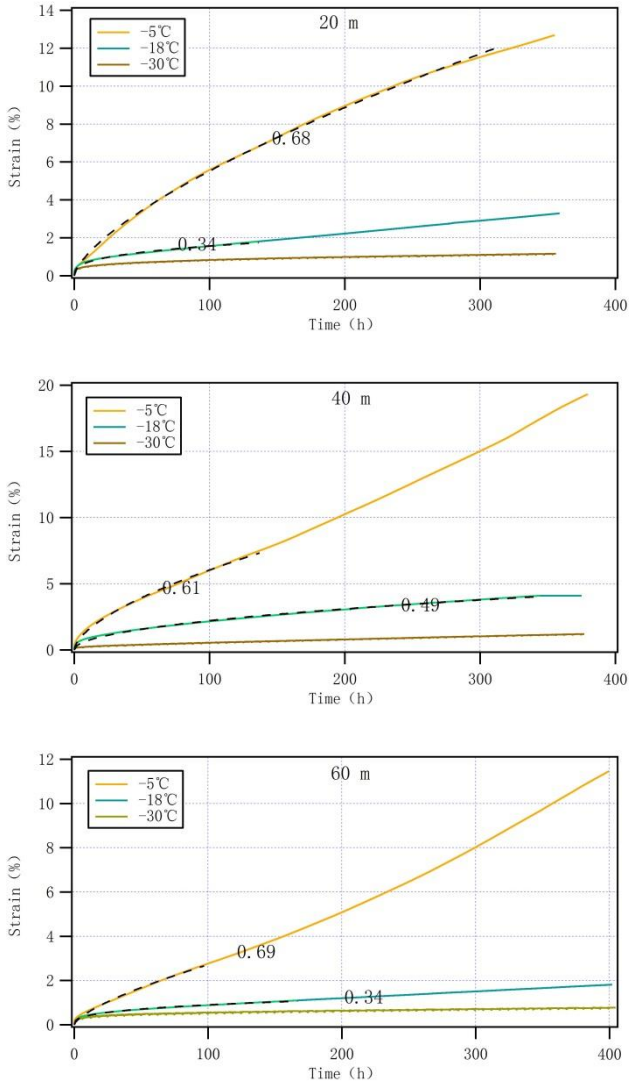

Figure 5: Strain vs. time for firn specimens at –5°C (yellow lines), –18°C (blue lines), and –30°C (brown lines), from depths of 20 m (applied stress 0.21 MPa), 40 m (0.32MPa) and 60 m (0.43MPa). The black dashed curves represent fits to a modified Andrade-like equation with the time exponents indicated on the curves, if any.

(0.68, 0.61, and 0.69), and at –18ºC from 40 m (0.49) are greater than 0.33, while the *k* value from the –18ºC specimens at 20 m (0.34) and 60 m (0.34) are close to 0.33 that is usually

obtained for full-density polycrystal ice. Interestingly, an evident relationship between the density of firn and the *k* values, regardless of the effect of stress (Li and Baker, 2022a) and temperature, remains unknown. A greater *k* value signifies faster deformation. The *k* values derived for firn are generally higher than those for polycrystalline ice, implying that the higher firn deformation rates compared to those of ice are likely related to the fewer grain-boundary constraints with more void space in firn (Li and Baker, 2022a; Li, 2023b). Clearly, the above *k* values, which increased with increasing temperature (**Figure 5**), indicate that deformation is easier because of the lower viscosity at the higher temperature. Thus, *k* seems to be a state variable with respect to temperature. In addition, *k* values greater than 0.33 may be related to the decrease of viscosity of the firn specimens (Freitag et al., 2002; Fujita et al., 2014). *k* values lower than 0.33 observed under constant load and temperature occurred at relatively low effective stresses (Li and Baker, 2022a). However, the steady decrease of *k* values from –5°C to –18°C remains further investigation. Alternatively, the enhanced cohesion strength in the firn, which resulted from both the ice matrix with higher purity and the stronger bond connection of inter-grains, increases the viscosity of test samples and lowers the *k* value to less than 0.33.

3.4 *Relationship of strain rate to strain*

Figure 6 shows log strain rate vs. strain plots from all the –5°C and –18°C specimens; the –30°C samples are excluded due to noise. The evolution of the strain rate is characterized more clearly in **Figure 6** than in **Figure 5**. Clearly, the strain rate is also a state variable of temperature, where the strain rate increases with increasing temperature for a given strain at a given depth (**Figure 6**; **Table 2**). The strain rate minimum at the secondary creep stage (SRmin) and the strain at the

Table 2. Observed and inferred strain rate minima and strains observed at the strain rate minima.

20 m	SRmin s^{-1}	PC1-SRmin s^{-1}	PC2-SRmin s^{-1}	PC3-SRmin s^{-1}	Strain %
–5°C	5.53×10^{-6}	***5.53×10⁻⁶***	*1.68×10⁻⁶*	*2.56×10⁻⁷*	11.8
–18°C	1.36×10^{-6}	***1.36×10⁻⁶***	*2.29×10⁻⁷*	*2.45×10⁻⁸*	1.81–2.9
–30°C(U)	–	7.14×10^{-7}	2.17×10^{-7}	3.3×10^{-8}	–
–30°C(L)	–	3.16×10^{-8}	9.6×10^{-9}	1.46×10^{-9}	–

40 m	SRmin s^{-1}	PC1-SRmin s^{-1}	PC2-SRmin s^{-1}	PC3-SRmin s^{-1}	Strain %
–5°C	1.03×10^{-5}	*3.39×10⁻⁵*	***1.03×10⁻⁵***	*1.57×10⁻⁶*	7.5
–18°C	1.4×10^{-6}	*8.32×10⁻⁶*	***1.40×10⁻⁶***	*1.5×10⁻⁷*	4.1
–30°C(U)	–	4.37×10^{-6}	1.33×10^{-6}	2.03×10^{-7}	–
–30°C(L)	–	1.94×10^{-7}	5.88×10^{-8}	8.97×10^{-9}	–

60 m	SRmin s^{-1}	PC1-SRmin s^{-1}	PC2-SRmin s^{-1}	PC3-SRmin s^{-1}	Strain %
–5°C	5.59×10^{-6}	*1.21×10⁻⁴*	*3.67×10⁻⁵*	***5.59×10⁻⁶***	2.7
–18°C	5.33×10^{-7}	*2.96×10⁻⁵*	*4.99×10⁻⁶*	***5.33×10⁻⁷***	1.1–1.8
–30°C(U)	–	1.56×10^{-5}	4.74×10^{-6}	7.21×10^{-7}	–
–30°C(L)	–	6.91×10^{-7}	2.1×10^{-7}	3.19×10^{-8}	–

The SRmin without the prefix is the observed values during creep, while the SRmin with a prefix is the inferred values. Note that PC-SRmin is the abbreviation of the post-calibration SRmin, and that –30°C(U) and –30°C(L) indicate the upper and lower bound from the –30°C samples from 44.8 kJ mol^{-1} and 113 kJ mol^{-1}, respectively. PC1-SRmin, PC2-SRmin, and PC3-SRmin are described in **Appendix B**. The symbol – indicates the unavailable values of SRmin and the strain value at the SRmin observed during creep. For the italics highlighted, see **Appendix B**.

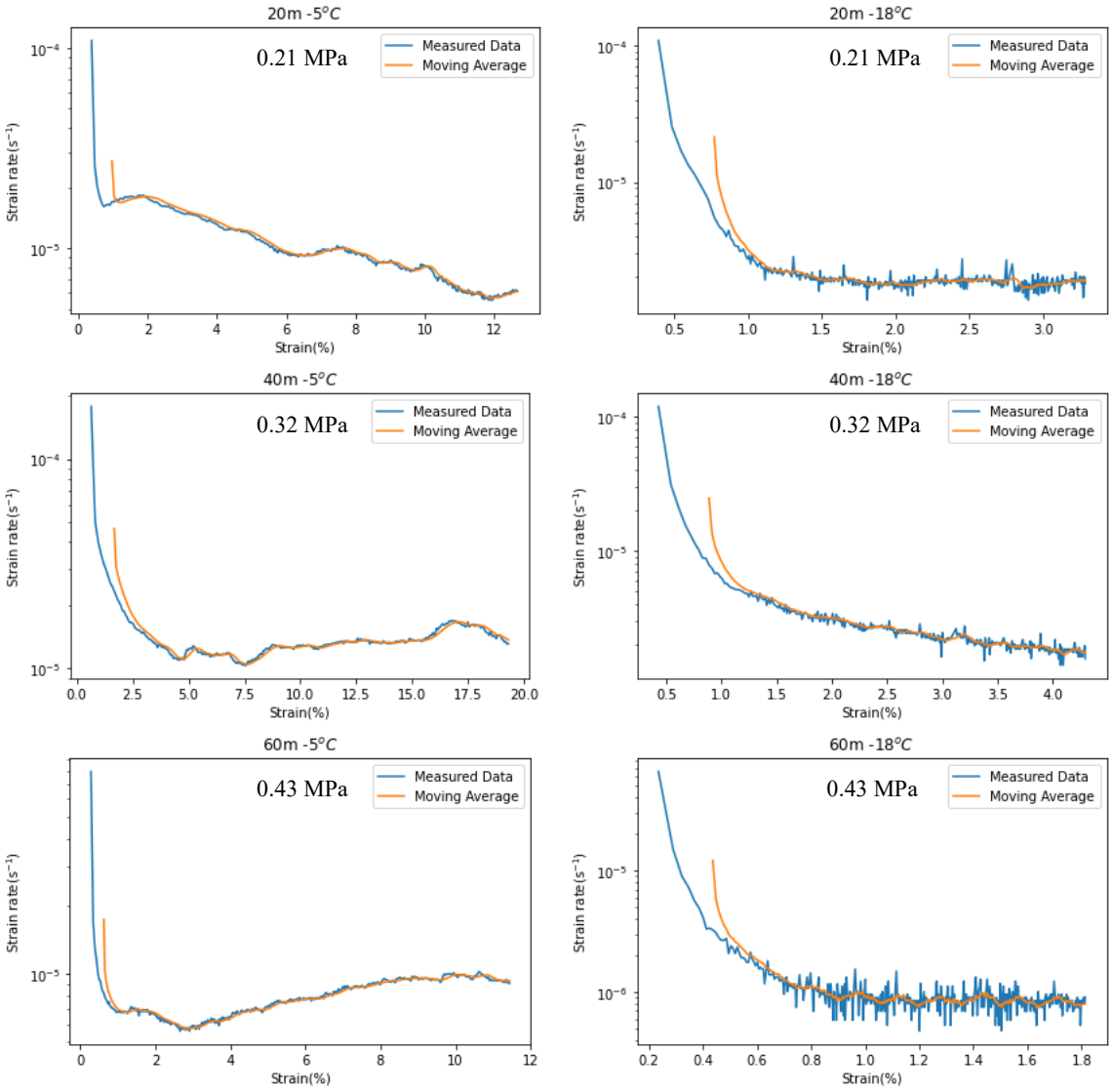

Figure 6: Log strain rate vs. strain from the firn specimens at temperatures of -5°C and -18°C from depths of 20 m (applied stress 0.21 MPa), 40 m (0.32MPa) and 60 m (0.43MPa). Samples from -30°C are not shown due to the very large noise. The blue lines represent discrete strain rates, which are calculated by extracting the strain data hourly, while the orange lines represent a moving average of 15 moving windows with respect to the strain.

SRmin for all the –5°C and –18°C specimens are shown in **Figure 6** and **Table 2**. The SRmin was reached at a strain of 11.8%, 7.5% and 2.7% for the –5°C specimens from depths of 20 m, 40 m,

and 60 m, respectively, consistent with strains at the SRmin decreasing with increasing depth at a given temperature in **Figure 8** and **Table 4** in Li and Baker (2022a). For the –18 °C specimens, the SRmin occurred over a range of strains from 1.81–2.9% at 20 m, at a fixed strain of 4.1% at 40 m, and at a strain oscillating between 1.1 and 1.8% at 60 m. These values of strain at different SRmin values are different from those usually observed at strains of 0.5–3% for fully-dense ice (Cuffey and Paterson, 2010, and references therein), implying different mechanical behavior between firn and pure ice (Duval, 1981; Mellor and Cole, 1983; Jacka, 1984; Li et al., 1996; Jacka and Li, 2000; Song et al., 2005, 2008; Cuffey and Paterson, 2010). Overall, the strain at the SRmin is greater with lower density and higher temperature, e.g. 11.8% strain from the –5°C specimens at 20 m, and 4.1% strain from the –18°C specimens at 40 m. This is likely due to the effect of strain hardening on density and temperature (Li, 2023b). Additionally, tertiary creep occurs both during quasi-steady state deformation (from the –5°C specimens at 40 m and 60 m) and in the ascending stage (from the –5°C and –18°C specimens at 20 m and the –18°C specimen at 40 m) more easily with lower firn density, greater effective stress, and higher creep temperature, e.g. from the –5°C specimens at 20 m, where the strain softening is primarily due to recrystallization (Duval, 1981; Jacka, 1984; Jacka and Li, 2000; Song et al., 2005; Faria et al., 2014) or the activated easy slip systems (Jonas and Muller, 1969; Duval and Montagnat, 2002; Alley et al., 2005; Horhold et al., 2012; Fujita et al., 2014; Eichler et al., 2017).

3.5 *Apparent activation energy for creep*

Experimental observations of the SRmin are limited, as they only occurred for the –5°C and at –18°C specimens at each depth (**Table 2**). It is hard to achieve the SRmin for all firn specimens in

laboratory environments (Landauer, 1958), especially under low temperatures and stresses such as those from the –30°C specimens in this work. To this end, we offer the various possibilities of the SRmin using the evidence we have. The value of the apparent activation energy of creep, Q_c (kJ mol^{-1}), is equal to the slope of a line fitted $\ln \dot{\varepsilon}$ versus $1/T$ as did in Goldsby & Kohlstedt (1997; 2001), using the Arrhenius relation $\dot{\varepsilon} = B\sigma^n \exp(-\frac{Q_c}{RT})$, where $\dot{\varepsilon}$ (s^{-1}) is the strain rate, B (s^{-1} Pa^{-n}) is the material parameter, σ (MPa) is the applied stress, n is the creep (stress) exponent, R (8.314 J mol^{-1} K^{-1}) is the gas constant, and T (K) is Kelvin temperature. First, the estimation of Q_c is based on *only* two SRmin values from the –5°C and –18°C samples at each depth (**Table 2**). From Glen-King's results deriving the activation energy (Glen, 1955) $\dot{\varepsilon}=A\exp(-Q_c/RT) = B\sigma^n \exp(-Q_c/RT)$, the pre-factor A, the material parameter B (Glen, 1955; Goldsby and Kohlstedt, 2001), and the stress exponent n (Li and Baker, 2022a) are assumed to be constant, as reported in the literature. The variability in density for the samples from 20-m depth on the mechanical behavior are negligible due to a small difference (up to ~4%), between samples, which falls within an acceptable error range in previous studies. This is likely related to multiple factors, including the intrinsic properties of the samples, e.g. inclusions (impurities, dust, bubbles, clathrate hydrates), the effects of deformation and partial annealing of firn due to stress distribution and temperature changes during drilling, extraction, transportation, or storage, and the fact that the samples are taken from adjacent parts of the core, and might capture heterogeneous density layers, as well as potential measurement errors associated with the equipment used. The Q_c values from the 20 m, 40 m, and 60 m specimens were calculated to be 61.4 kJ mol^{-1}, 87.3 kJ mol^{-1}, and 102.8 kJ mol^{-1}, respectively (**Figure 7**). Based on the three SRmin from the –5°C and –18°C samples at 60 m in this work, and from –10°C samples at 60 m in Li and Baker (2022a), a

438 Q_c value for the 60 m specimen was calculated to be 100.7 kJ mol^{-1}. To see whether or not these
439 above Q_c values are reliable, we estimated the activation energy of grain-boundary
440 diffusion/viscosity, Q_{gbd} (kJ mol^{-1}), using the relation $K = \left(D_t^2 - D_0^2\right)/t = k\exp(-Q_{gbd}/RT)$,
441 in an alternative form of $Q_{gbd} = -R\left[\partial \ln K/\partial\left(1/T\right)\right]$, where K is the observed rate of grain
442 growth (mm^2 a^{-1}), D_0^2 and D_t^2 are the measured mean grain area (mm^2) in a firn sample at the
443 onset of the creep (t = 0), and at the end time of the creep (t-year), and k is a constant grain
444 growth factor. The grain growth rates are plotted on a logarithmic scale against the reciprocal of T
445 (**Figure 7**). For changes in grain size from the related specimens before and after creep see **Table**
446 **3**. Correspondingly, the Q_{gbd} values calculated were 41.4 kJ mol^{-1}, 40.8 kJ mol^{-1}, and 40.9 kJ
447 mol^{-1} for the specimens at 20 m, 40 m, and 60 m, respectively. These Q_{gbd} values are comparable
448 to the values of 40.6 kJ mol^{-1} obtained in laboratory experiments on polycrystalline ice (Jumawan,
449 1972), and 42.4 kJ mol^{-1} from 13 polar firn cores (Cuffey and Paterson, 2010) for grain-boundary
450 self-diffusion of polycrystalline ice. Further, the ratio of Q_{gbd}/Q_c is 0.67, 0.47, and 0.4 for the 20 m,
451 40 m, and 60 m specimens, respectively. We noted that the ratio of 0.67 for Q_{gbd}/Q_c was
452 recommended by Hobbs (1974) and Cuffey and Paterson (2010). The Q_c values calculated using
453 the Arrhenius relation for the 40 m and 60 m specimens are likely greater than the actual values,
454 and hence are seemingly less reliable. There is little difference between the two-SRmin-derived
455 Q_c value (102.8 kJ mol^{-1}) and the three-SRmin-derived Q_c value (100.7 kJ mol^{-1}), implying
456 that these two avenues for calculating Q_c have equal utility. Moreover, the above Q_{gbd} values
457 are lower than the 48.6 kJ mol^{-1} that was inferred by the grain growth rate for firn samples with
458 densities ranging from 320–650 kg m^{-3} from cores drilled at the South Pole, Antarctic (Gow,
459 1969), which makes a ratio of 0.67 for Q_{gbd}/Q_c an unreliable sole-criterion. In short, it is difficult

to assess the reliability of both Q_c and Q_{gbd}, as discussed above due to their scatter and debates in the current literature. Thus, these Q_c values estimated in this work, ranging from 61.4–102.8 kJ mol^{-1}, are reasonable, aligning with the literature range of 44.8–113 kJ mol^{-1} (**Table 4**).

Table 3. Grain area (mm^2) measured from optical thin sections for samples at –5°C, –18°C, and –30°C from depths of 20 m, 40 m, and 60 m before and after creep.

Depth	20 m		40 m		60 m	
T/°C	Before	After	Before	After	Before	After
–5	0.29±0.25	0.42±0.28	0.53±0.32	0.79±0.67	0.78±0.67	0.97±0.8
–18	0.29±0.25	0.34±0.2	0.53±0.32	0.7±0.42	0.78±0.67	0.9±0.59
–30	0.29±0.25	0.31±0.17	0.53±0.32	0.57±0.34	0.78±0.67	0.81±0.56

A great challenge is the estimation of the Q_c using the SRmin including the –30°C specimens, whose SRmin shows high variability due to the extraordinarily slow strain rate at low temperatures. This difficulty cannot be resolved by extrapolating experimental data (Sinha, 1978; Hooke et al., 1980), e.g. the use of Andrade's law (Glen, 1955). Instead, we turned our focus to studying the relationship between the SRmin and temperature by constraining our data in a wide range of Q_c values reported in existing literature presented in **Table 4**. Clearly, there is a larger scatter of Q_c values for firn than for ice. The increase of Q_c from mono-crystalline and bi-crystalline to polycrystalline ice implies that the greater the reduction in the constraint from grain boundaries, the greater is Q_c. Alternatively, firn creep is easier than that of polycrystalline ice due to either the easier sliding of grains in firn along more directions in the more porous and heterogeneous structure (Section 3.3), or the decrease of viscosity associated with inclusions (e.g.

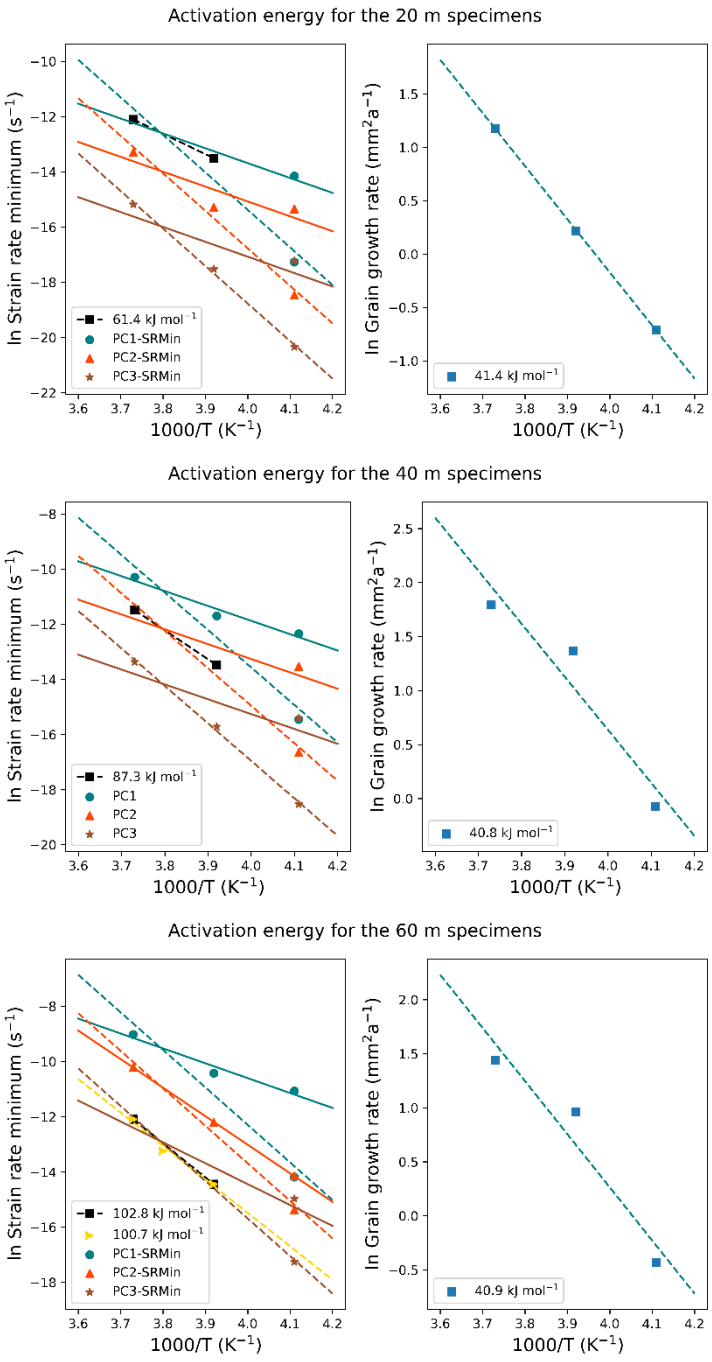

Figure 7: Arrhenius plots to estimate the apparent activation energy of creep (Q_c; left panel) and the apparent activation energy of grain-boundary diffusion (Q_{gbd}; right panel) from the firn specimens noted. The teal, orange, and brown solid lines are the upper bound (44.8 kJ mol^{-1}) of PC1-SRmin, PC2-SRmin, and PC3-SRmin, respectively, while the teal, orange, and brown dashed

lines are the lower bound (113 kJ mol^{-1}) of PC1-SRmin, PC2-SRmin, and PC3-SRmin, respectively (Table 2). The teal circles, the orange triangles, and the brown stars are the data in Table 2. The black dashed lines are from *only* two SRmins at –5°C and –18°C (the black squares are the data measured), whose Q_c is indicated in each subfigure. The yellow dashed line is from the three SRmins at –5°C, –18°C in this work, and –10 °C from Li and Baker (2022a) (the yellow triangles are the measured data), whose Q_c is 110.7 kJ mol^{-1}. The blue dashed lines (right panel) are from grain growth rate at three temperatures (the blue squares are the observed data), whose Q_{gbd} is indicated in each subfigure.

Table 4. Apparent activation energy for the creep of firn and ice, Q_c, reported in literature.

Q_c kJ mol^{-1}	Sample	Density kg m^{-3}	Temperature °C	Methods	Source
58.6–113	Firn	~400	[–13.6, –3.6]	Uniaxial/Hydrostatic Compression	Landauer (1958)
44.8–74.5	Firn/Bubbly Ice	440–830	[–34.5, –0.5]	Uniaxial Unconfined Compression	Mellor and Smith (1966)
54	Firn/Bubbly Ice	Undetailed	[−28, −16]	Shear Deformation of Boreholes	Paterson (1977)
~72.9	Firn	320–650	Unnecessary	Grain Growth Rate	Gow (1969)
69 ± 5	Firn	423 ± 8	[–19, –11]	Triaxial Compression	Scapozza and Bartelt (2003)
~60	Artificial/Natural Ice (South Pole)	~917	–15	Torsion Creep Test	Pimienta and Duval (1987)
61	Polycrystalline Ice	~917	–9.6	Hydrostatic Pressure	Duval et al. (1983)
78	Monocrystalline Ice	~917	[–30, –4]	Derived from Bicrystal Ice	Homer and Glen (1978)
75	Ice Bicrystal	~917	[–30, –4]	Tensile Test Parallel to Grain-boundary	Homer and Glen (1978)

Baker and Gerberich, 1979; Goodman et al., 1981) that facilitate the intra- and inter-grain sliding (Salamatin et al., 2009). In principle, Q_c of firn should exceed that for polycrystalline ice. Intriguingly, some reported Q_c values from firn are less than that for ice, meaning the degree of spatial freedom in the ice-matrix is limited by the topological structure of the firn (Liu et al., 2022). Incidentally, the effective stress of porous materials is determined by not only its porosity, but also other factors, e.g. the microstructural topology (Liu et al., 2022) and the impurity types and concentrations in the firn. However, this issue is beyond the scope of this work. In summary, a Q_c for firn, which ranges from 44.8–113 kJ mol^{-1}, is plausible due to the intrinsic nature of natural firn that has a far more complicated and changeable microstructure than ice.

The value of the stress exponent *n* is determined by plotting the line fit the logarithm relation of the steady-state strain rate, $\dot{\varepsilon}$, versus the effective stress, σ, and is, thus, the slope of this line from the measured SRmins (**Table 2**). We found *n* to be ~0.1 and ~ –1.2 for the –5°C and –18°C samples, respectively, which contradicts the reported *n* = ~4.3 by Li and Baker (2022a) and other values around 3 (Glen, 1955; Kamb, 1961; Raymond, 1973; Thomas et al., 1980; Weertman, 1985; Goldsby and Kohlstedt, 2001; Cuffey, 2006). This significant discrepancy implies that the uncalibrated SRMin value from all of the samples is not appropriate for estimating the stress exponent, and hence the activation energy during their deformation. To proceed, the post-calibration SRmins for the –5°C and –18°C samples are highlighted in **Table 2** (see **Appendix B** in detail). It is important to note that the stress exponent does not depend on the density of the tested samples, thereby negating any basis for discussing a relationship between the

523 stress exponent and sample density. Instead, variations in stress corresponding to density
524 variations are manifested in the strain rate, ensuring that the derivation of the stress exponent and
525 activation energy remains consistent. From here on we only discuss the applied stress since there
526 is little difference between the effective stress and applied stress for calculating the stress
527 exponent (Li and Baker, 2022a). Based on both the reported range of Q_c and the two observed
528 SRmins at −5°C and −18°C, the SRmins for the −30°C samples are inferred (**Table 2**), using the
529 Arrhenius relation. Also, based on both the observed and inferred SRmins with the upper and
530 lower bounds (**Table 2**), a series of fitted functions are then found between the SRmin and the
531 reciprocal of the temperature (°C), $1/T_c$:
532
533 20-m samples:
534
$$\begin{cases} \mathrm{SRMin} = -3\times10^{-5}/\mathrm{T_c} - 7\times10^{-7}[\mathrm{R}^2 = 0.988; \mathrm{PC1(L\,20)}] \\ \mathrm{SRMin} = -3\times10^{-5}/\mathrm{T_c} - 2\times10^{-7}[\mathrm{R}^2 = 1; \mathrm{PC1(U\,20)}] \\ \mathrm{SRMin} = -1\times10^{-5}/\mathrm{T_c} - 3\times10^{-7}[\mathrm{R}^2 = 1; \mathrm{PC\,2(L\,20)}] \\ \mathrm{SRMin} = -9\times10^{-6}/\mathrm{T_c} - 2\times10^{-7}[\mathrm{R}^2 = 0.987; \mathrm{PC\,2(U\,20)}] \\ \mathrm{SRMin} = -2\times10^{-6}/\mathrm{T_c} - 6\times10^{-8}[\mathrm{R}^2 = 0.998; \mathrm{PC\,3(L\,20)}] \\ \mathrm{SRMin} = -1\times10^{-6}/\mathrm{T_c} - 3\times10^{-8}[\mathrm{R}^2 = 0.976; \mathrm{PC\,3(U\,20)}] \end{cases},$$

535 40-m samples:
536
$$\begin{cases} \mathrm{SRMin} = -2\times10^{-4}/\mathrm{T_c} - 4\times10^{-6}[\mathrm{R}^2 = 0.988; \mathrm{PC1(L\,40)}] \\ \mathrm{SRMin} = -2\times10^{-4}/\mathrm{T_c} - 2\times10^{-6}[\mathrm{R}^2 = 1; \mathrm{PC1(U\,40)}] \\ \mathrm{SRMin} = -6\times10^{-5}/\mathrm{T_c} - 2\times10^{-6}[\mathrm{R}^2 = 1; \mathrm{PC\,2(L\,40)}] \\ \mathrm{SRMin} = -6\times10^{-5}/\mathrm{T_c} - 1\times10^{-6}[\mathrm{R}^2 = 0.987; \mathrm{PC\,2(U\,40)}] \\ \mathrm{SRMin} = -1\times10^{-5}/\mathrm{T_c} - 3\times10^{-7}[\mathrm{R}^2 = 0.998; \mathrm{PC\,3(L\,40)}] \\ \mathrm{SRMin} = -9\times10^{-6}/\mathrm{T_c} - 2\times10^{-7}[\mathrm{R}^2 = 0.976; \mathrm{PC\,3(U\,40)}] \end{cases},$$

537 60-m samples:

538
$$\begin{cases} \mathrm{SRMin} = -7\times10^{-4}/\mathrm{T_c} - 2\times10^{-5}[\mathrm{R}^2 = 0.988; \mathrm{PC1(L\,60)}] \\ \mathrm{SRMin} = -6\times10^{-4}/\mathrm{T_c} - 6\times10^{-6}[\mathrm{R}^2 = 1; \mathrm{PC1(U\,60)}] \\ \mathrm{SRMin} = -2\times10^{-4}/\mathrm{T_c} - 7\times10^{-6}[\mathrm{R}^2 = 1; \mathrm{PC\,2(L\,60)}] \\ \mathrm{SRMin} = -2\times10^{-4}/\mathrm{T_c} - 4\times10^{-6}[\mathrm{R}^2 = 0.987; \mathrm{PC\,2(U\,60)}] \\ \mathrm{SRMin} = -3\times10^{-5}/\mathrm{T_c} - 1\times10^{-6}[\mathrm{R}^2 = 0.998; \mathrm{PC\,3(L\,60)}] \\ \mathrm{SRMin} = -3\times10^{-5}/\mathrm{T_c} - 7\times10^{-7}[\mathrm{R}^2 = 0.976; \mathrm{PC\,3(U\,60)}] \end{cases},$$

539

540 where PC1(L20) and PC1(U20) indicate the lower and upper bound values of the post-calibration
541 SRmins from the 20 m samples (**Table 1**), and other symbols are similarly formatted, e.g.
542 PC1(L40), PC1(U40), PC1(L60), PC1(U60), and so on. These relationships are plotted in **Figure**
543 **8**, where the SRmin vs. $1/T_c$ plots from the three depths are almost the same shape, implying that
544 the SRmin is dependent on the temperature at a constant stress. It is important to note that the
545 average (minimum) strain rate for the secondary creep stage for a given temperature increases
546 with increasing depth/density of the samples (**Figure 8**; **Table 2**). This is opposite to a decrease of
547 the SRmin at a fixed stress and temperature in **Figure 8** and **Table 4** in Li and Baker (2022a).
548 These changes in SRmin are irrespective of the stress (**Appendix A**). The temperature plays a
549 predominant role during firn creep for a given density of sample at a constant stress. An
550 interesting question on firn creep at a specific temperature is whether the SRmin slows down or
551 speeds up with decreasing density of firn. Certainly, natural firn samples raise the complexity in
552 interpreting the firn creep due to the influences both from inclusions (Li and Baker, 2022a and
553 references therein; Li, 2024), and from the topology of the microstructures (Liu et al., 2022). In
554 addition, there is a broad spread of the SRmin at each depth, in which the SRmin varies by several
555 times, even one order of magnitude or more between the different possibilities of post-calibration
556 SRmins (**Figure 8**), implying that the microstructure of the sample significantly influences the

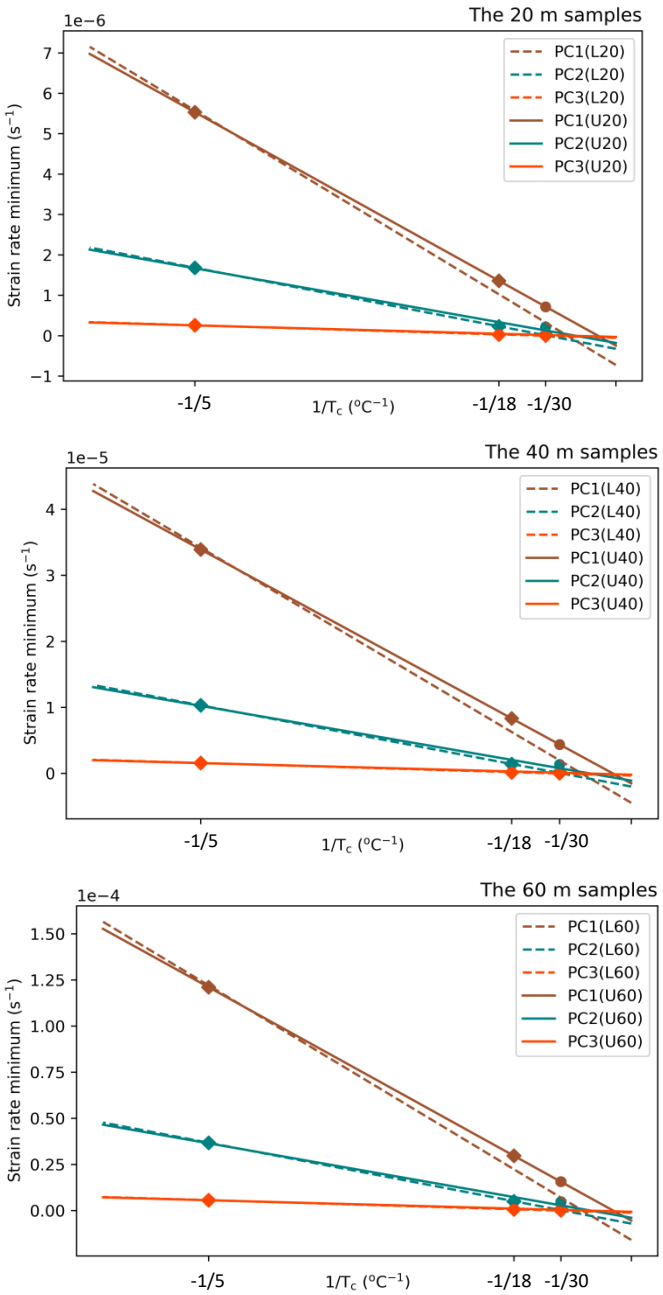

Figure 8: Plots of the strain rate minimum versus the reciprocal of temperature. PC1(L20) and PC1(U20) indicates the lower and upper bound, respectively, from the 20 m samples via PC1 as noted in Table 2, and so on. The circles indicate the upper bound data measured and inferred, while the squares indicate the lower bound data. The dashed line is the fit from the lower bound, while the solid line is the fit from the upper bound.

process of the creep of firn. Moreover, it is hard to generalize a universal formula for predicting the SRmin at temperatures below −30°C, where the SRmins becomes negative (**Figure 8**). Thus, there is a need for an in-depth understanding of the polar firn creep behavior in secondary creep stage.

To illustrate the differences between the Q_c values calculated from PC1-SRmin, PC2-SRmin, and PC3-SRmin, we have plotted them in **Figure 7**. Interestingly, the Arrhenius plots of the natural logarithm of strain rate with 1000/T (**Figure 7**) are similar to those observed by Glen (1955) and Homer and Glen (1978), implying that there is no significant difference in the creep mechanism for a temperature range of –30 ^{o}C to –5 ^{o}C (Glen, 1955; Homer and Glen, 1978), where both diffusion via grain-boundary, vacancy or interstitial defects (Barnes et al., 1971; Brown and George, 1996; Nasello et al., 2005; Li and Baker, 2022b), and dislocations contribute to the creep of polar firn.

4. Conclusions

Constant-load creep tests were performed on three cylindrical specimens tested from depths of 20 m (applied stress 0.21 MPa), 40 m (0.32 MPa) and 60 m (0.43 MPa) at temperatures of –5 ± 0.2^{o}C, –18 ± 0.2^{o}C, and –30 ± 0.2^{o}C from a firn core extracted at Summit, Greenland in June 2017. The microstructures were characterized before and after creep testing using the micro-CT and thin sections viewed between optical crossed polarizers. It was found that:

1. Microstructural parameters measured using the micro-CT show that the polar firn densified during the creep compression (e.g. from 685 to 729 kg m^{-3} for the 40 m specimen at –5°C), *viz.*, the TP (from 25.5 to 20.7%), the ECDa (from 0.86 to 0.69 mm), the SSA (from 3.26 to 3.02 mm^{-1}), and the SMI (from –1.85 to –2.8) decreased, while the S.Th (from 0.95 to 0.99 mm) and the CP (from 0.01 to 0.02%) increased. Anomalies in the microstructures, especially at low temperatures of –18°C and –30°C, are likely due to metamorphism under temperature gradients, the radial dilation effect during firn deformation, the measurement uncertainty of the micro-CT, or the anisotropy and the heterogeneity of natural firn.
2. The transient creep behavior of firn at constant stress and different temperatures obeys an Andrade-like law, but, the time exponent k of 0.34–0.69 is greater than the 0.33 found for ice. This is due to fewer grain-boundary constraints in porous firn than in ice.
3. The secondary creep behavior of firn at constant stress and different temperatures presented here shows that the strain at the SRmin increases with decreasing firn density and increasing creep temperature. In particular, low-density firn during creep at high temperatures shows that the strain at the SRmin, e.g. 11.8% and 7.5% respectively from the 20 m and 40 m specimens at –5°C, is greater than the strain of 3%, which is the maximum found at the SRMin of ice.
4. The tertiary creep behavior of firn at constant stress and different temperatures is more easily observed from lower-density specimens at greater effective stresses and higher creep temperatures. The strain softening in tertiary creep is primarily due to recrystallization.
5. The apparent activation energy for the firn creep has a wide range of 61.4–102.8 kJ mol^{-1} because the grains in firn slide more easily along more directions in the more porous and heterogeneous structure, the enhanced fluidity from inclusions, and the topological structure

of the firn. In addition, the SRmin is a function of the temperature, depending on the microstructure of firn and the inclusion content. The predicted SRmin increases with increasing firn density at a given temperature and is independent of the effective stress. Lastly, there is no significant difference in the creep mechanism at temperatures ranging from –30°C to –5°C.

The creep of polar firn behaves differently from full-density ice, implying that firn densification is an indispensable process in fully understanding the transformation of snowfall to ice in the polar regions. Observed firn deformation indicates that temperature plays a determined role in firn densification. Thereby, it will be helpful to bridge a gap between the firn temperature and the climate of the past for reconstructing paleoclimate. Also, it will be helpful to apply a confining load to investigate the microstructure of the creep of polar firn with smaller initial particle sizes at low temperatures using the micro-CT. Further studies of interest are to investigate the quantitative relationship between the microstructural parameters and the mechanical behavior of polar firn, and when the onset of recrystallization occurs during creep, as well as verify the SRmin predicted by the relationship of SRmin vs. temperature from the firn specimens at more extensive ranges of stresses and temperatures.

Appendix A: Hydrostatic pressure, the applied stress, and the effective stress

The hydrostatic pressure, p, was calculated from the overburden pressure of snow, using $p=\bar{\rho}_f gh$, where $\bar{\rho}_f$ is the average firn density above the depth of interest, *h*, and *g* is the acceleration of gravity. At Summit, p at the depths of 20 m, 40 m, and 60 m was estimated to be ~0.1 MPa, ~0.22 MPa, and ~0.38 MPa, respectively. Note that the slope of the surface of ice sheets and glaciers at Summit is idealized to be zero, i.e., their surfaces are horizontal. The applied stress, σ, is the applied load divided by the cross-sectional area of a sample. The σ at the depths of 20 m, 40 m, and 60 m were 0.21 MPa, 0.32 MPa, and 0.43 MPa, respectively. The effective stress, $\tilde{\sigma}$, is defined as σ divided by the fraction of ice matrix in firn, see in detail from Li and Baker (2022a). Thereby, $\tilde{\sigma}$ is 0.32 MPa (the mean porosity of 34.9%), 0.43 MPa (24.8%), and 0.5 MPa (14.4%) from the 20–60 m samples, respectively. Note that the stresses were vertically loaded on the sample (parallel to the direction of core axis of the sample) in laboratory tests. Ideally, in order to be analogous to the densification of firn in nature, $\tilde{\sigma}$ for laboratory samples from a given depth should be equal to the p of firn *in situ* at an equivalently same depth at Summit, namely $\tilde{\sigma}$/p = 1. However, in consideration of the laboratory timeframe for experiments (Pimienta and Duval, 1987), the stresses applied in laboratory tests are usually higher with a resulting higher rate of deformation than those *in situ*. Thus, to observe the effect of the stress on the creep of firn with different densities at different depths, we designed the following configuration of the $\tilde{\sigma}$/p with depth, *viz.*, 0.32 MPa/~0.1 MPa = ~3.2, 0.43 MPa/~0.22 MPa = ~1.95, and 0.5 MPa/~0.38 MPa = ~1.32 for the samples from the depths of 20 m, 40 m, and 60 m, respectively. In this manner, the decrement of $\tilde{\sigma}$/p with increasing depth represents the decrease of the effective stress with increasing depth. Also, it's important to note that the strain rates

achieved during creep experiments in laboratory settings are 6 to 7 times faster than on ice sheets due to the constraints of conducting experiment in reasonable times, which requires higher loads.

Appendix B: Strain rate minimum inferred via two kinds of constraints

To improve the reliability of inferred SRmins, two kinds of constraints were applied. First, the SRmins from the –5°C and –18°C samples are calibrated using Glen's law $\dot{\varepsilon}=A\sigma^{n}$ with n = 4.3 (Li and Baker, 2022a). PC1-SRmin, PC2-SRmin, and PC3-SRmin indicate three possibilities of the SRmins that are calculated from the 20 m, 40 m, and 60 m samples via the *only* SRmin observed at a given temperature (Table 2). As an example, for the –5°C samples, there exist three possibilities from three depths. 1) The SRmin observed from the 20 m sample in bold italic font is used to calculate two other SRmins for the 40 m and 60 m samples in the italic font in the column of PC1-SRmin. 2) In the same manner as in scenario 1), the SRmin observed from the 40 m sample is calculated in the column of PC2-SRmin in the bold italic font, and the SRmin observed from the 60 m sample is calculated in the column of PC3-SRmin in the bold italic font. 3) In the same manner as in scenarios 1) and 2), the SRmin is calculated for the –18 °C samples in turn from three depths. Second, the SRMin of the –30°C samples is inferred on the basis of the range of Q_c, i.e., from 44.8 kJ mol^{-1} (upper bound) to 113 kJ mol^{-1} (lower bound), using the Arrhenius relation.

Data availability

The data supporting the conclusions in this study are available at https://arcticdata.io/catalog.

Author contribution

YL and IB designed the experiments and YL carried them out. YL analyzed the data and visualized the relevant results. YL prepared the manuscript with contributions from all co-authors.

Competing interests

At least one of the (co-)authors is a member of the editorial board of The Cryosphere.

Acknowledgements

This work was sponsored by the National Science Foundation Arctic Natural Science grant 1743106. Y. L. is grateful to Ciao Fu for the great support and help in COVID-19. The authors wish to thank Chris Polashenski, Zoe Courville and Lauren B. Farnsworth at USA-CRREL for their help with storage of the firn cores. The authors acknowledge the use of the Ice Research Laboratory (Director-Erland Schulson) at Dartmouth College.

References:

Adolph, A.C.C., Albert, M.R., 2014. Gas diffusivity and permeability through the firn column at Summit, Greenland: measurements and comparison to microstructural properties. T. Cryosph., 8, 319–328, doi:10.5194/tc-8-319- 2014.

Albert, M.R., Shultz, E.F. and Perron, F.E., 2000. Snow and firn permeability at Siple Dome, Antarctica. Ann. Glaciol. 31, 353-356.

Alley, R.B., Clark, P.U., Huybrechts, P., Joughin, I., 2005. Ice-sheet and sea-level changes. Sci. 310(5747), 456-60. doi: 10.1126/science.1114613. PMID: 16239468.

Ambach, W., Eisner, H., 1985. Rheological properties of temperate firn. Polarforschung, Bremerhaven, Alfred Wegener Institute for Polar and Marine Research & Germany Society of Polar Research 55(2), 71–77. hdl:10013/epic.29564.d001.

Anderson, D.L., Benson, C.S., 1963. The densification and diagenesis of snow. In: Kingery, W.D. (Ed.), Ice and Snow. Press, Cambridge, Massachusetts, M.I.T, pp. 391–411.

Arnaud, L., Gay, M., Barnola, J.M., Duval P., 1998. Imaging of firn and bubbly ice in coaxial reflected light: a new technique for the characterization of these porous media. J. Glaciol., 44(147), 326-332.

Ashby, M.F., Duval, P. 1985. The creep of polycrystalline ice. Cold Reg. Sci. Technol., 11 (3), 285-300. doi:10.1016/0165-232X(85)90052-7.

Baker, R.W., Gerberich, W.W., 1979. The effect of crystal size and dispersed-solid inclusions on the activation energy for creep of ice. J. Glaciol., 24(90), 179-194.

Barnes, P., Tabor, D., Walker, J.C.F., 1971. The friction and creep of polycrystalline ice. Proc. Roy. Soc. Lond. A (324),127-155.

718 Bartelt, P., Von Moos, M., 2000. Triaxial tests to determine a microstructure-based snow viscosity
719 law. Ann. Glaciol., 31, 457-462.
720 Brown, D.E., George, S.M., 1996. Surface and bulk diffusion of $H_2{}^{18}O$ on single-crystal $H_2{}^{16}O$ ice
721 multilayers. J. Phys. Chem. 100 (38) 15460–15469.
722 Budd, W.F., Jacka, T.H., 1989. A review of ice rheology for ice sheet modelling. Cold Reg. Sci.
723 Technol. 16(2), 107–144. doi: 10.1016/0165-232X(89)90014-1.
724 Burr, A., Ballot, C., Lhuissier, P., Martinerie, P., Martin, C.L., Philip, A., 2018. Pore morphology
725 of polar firn around closure revealed by X-ray tomography, T. Cryosphy., Copernicus, 12(7),
726 2481-2500. 10.5194/tc-12-2481-2018. hal-01864373.
727 Coleou, C., Lesaffre, B., Brzoska, J.B., Ludwig, W., Boller, E., 2001. Three-dimensional snow
728 images by X-ray microtomography, Ann. Glaciol., 32, 75-81.
729 Courville, Z., Horhold, M., Hopkins, M. and Albert, M., 2010. Lattice-Boltzmann modeling of the
730 air permeability of polar firn. J. Geophys. Res., Earth Surface, 115(F4).
731 Gow, A.J., 1969. On the rates of growth of grains and crystals in South Polar firn. J. Glaciol., 8(53)
732 241-252.
733 Cuffey, K.M., 2006. Manifestations of ice microphysical processes at the scale of whole ice sheets.
734 In: Knight, P. (Ed.), Glacier Science and Environmental Change. Blackwell Publishing, 290–
735 300.
736 Cuffey, K.M., Paterson, W.S.B., 2010. The Physics of Glaciers, 4th edited. Elsevier Inc.
737 Durham, W.B., Stern, L.A., 2001. Rheological properties of water ice applications to satellites of
738 the outer planets. Annu. Rev. Earth Planet. Sci. 29(1), 295–330.
739 Duval, P., 1981. Creep and fabrics of polycrystalline ice under shear and compression. J. Glaciol.
740 27, 129–140.

741 Duval, P. Ashby, M.F., Anderman, I., 1983. Rate-controlling processes in the creep of
742 polycrystalline ice. The Journal of Physical Chemistry, 87, 4066-4074.
743 Duval, P., Montagnat, M., 2002. Comment on 'Superplastic deformation of ice: experimental
744 observations' by D. L. Goldsby and D. L. Kohlstedt. J. Geophys. Res.: Solid Earth. 107(B4),
745 ECV 4-1–ECV 4-2. doi: 10.1029/2001JB000946.hal-01698732.
746 Ebinuma, T., Maeno, N., 1987. Particle rearrangement and dislocation creep in a snow
747 densification process. J Phys.(Paris), 48,Colloq. C1, 263–269.
748 Eichler, J., 7 others, 2017. Location and distribution of micro-inclusions in the EDML and NEEM
749 ice cores using optical microscopy and in situ Raman spectroscopy. The Cryosphere. 11(3),
750 1075–1090. doi: 10.5194/tc-11-1075-2017.
751 Faria, S.H., Weikusat, I., Azuma, N., 2014. The microstructure of polar ice. Part II: state of the art.
752 J. Struct. Geol. 61, 21–49. doi:10.1016/j.jsg.2013.11.003.
753 Flin, F., Brzoska, J.B., Lesaffer, B., Coleou, C., Pieritz, R.A., 2004. Three-dimensional geometric
754 measurements of snow microstructural evolution under isothermal conditions. Ann. Glaciol.,
755 38, 39-44.
756 Freitag, J., Dobrindt, U., Kipfstuhl, J., 2002. A new method for predicting transport properties of
757 polar firn with respect to gases on the pore-space scale, Ann. Glaciol., 35, 538-544.
758 Frost, H.J., Ashby, M.F. 1982. Deformation-mechanism maps: the plasticity and creep of metals
759 and ceramics. Oxford: Pergamon Press.
760 Fujita, S., Hirabayashi, M., Goto-Azuma, K., Dallmayr, R., Satow, K., Zheng, J., Dahl-Jensen, D.,
761 2014. Densification of layered firn of the ice sheet at NEEM, J. Glaciol., 60 (223), 905-921,
762 doi:10.3189/2014JoG14J006.
763 Glen, J.W., 1955. The creep of polycrystalline ice, Proceedings of the Royal Society A, 228(1175),
764 519-538, doi.10.1098/rspa.1955.0066.

765 Goldsby, D.L., Kohlstedt, D.L., 1997. Grain boundary sliding in fine-grained ice I. Scr. Mater.
766 37(9), 1399–1406.

767 Goldsby, D.L., Kohlstedt, D.L., 2001. Superplastic deformation of ice: experimental observations,
768 J. Geophys. Res., 106(B6), 11017-11030.

769 Goodman, D.J., Frost, H.J., Ashby, M.F., 1981. The plasticity of polycrystalline ice, Philos. Mag.,
770 A43 665–695.

771 Hammonds, K., Baker, I., 2016. The effects of Ca++ on the strength of polycrystalline ice. J.
772 Glaciol. 62,1–9. doi: 10.1017/jog.2016.84.

773 Hammonds, K., Baker, I., 2018. The effects of H_2SO_4 on the mechanical behavior and
774 microstructural evolution of polycrystalline Ice. J. Geophys. Res.: Solid Earth. 123,1–22. doi:
775 10.1002/2017JF004335.

776 Hildebrand, T., Ruegsegger, P. 1997. A new method for the model-independent assessment
777 ofthickness in three-dimensional images. J. Microsc., 185, 67-75.

778 Hobbs, P.V., 1974. Ice Physics, 1st edited. Oxford University Press Inc., New York.

779 Homer, D.R., Glen, J.W., 1978. The creep activation energies of ice. J. Glaciol., 21(85), 429-444.

780 Hooke, R.L., Mellor, M., Budd, W.F., Glen, J.W., Higashi, A., Jacka, T.H., Jones, S.J., Lile, R.C.,
781 Martin, R.T., Meier, M.F., Russell-Head, D.S., Weertman, J., 1980. Mechanical properties of
782 polycrystalline ice: an assessment of current knowledge and priorities for research. Cold Reg.
783 Sci. Technol., 3, 263-275.

784 Hooke, R.L., 2005. Principles of Glacier Mechanics. Cambridge: Cambridge University Press.

785 Horhold, M.W., 5 others, 2012. On the impact of impurities on the densification of polar firn.
786 Earth Planet. Sci. Lett. 325–326,93–99. doi: 10.1016/j.epsl.2011.12.022

787 Jacka, T.H. 1984. The time and strain required for development of minimum strain rates in ice.
788 Cold Reg. Sci. Technol., 8 (3), 261-268. doi: 10.1016/0165-232X(84)90057-0.

789

790 Jacka, T.H., Li, J., 2000. Flow rates and crystal orientation fabrics in compression of
791 polycrystalline ice at low temperatures and stresses, Physics of Ice Core Records
792 International Symposium on Physics of Ice Core Records. Shikotsukohan, Hokkaido, Japan,
793 83-102.
794 Jonas, J.J., Muller, F., 1969. Deformation of ice under high internal shear stresses. Can. J. Earth
795 Sci. 6(4), 963–968. doi: 10.1139/e69-100.
796 Jumawan, A.B., 1972. An experimental study of self-diffusion in polycrystalline ice. Diss.Abstr.
797 Int. B 32, 5163–5164 (Abstract).
798 Kamb, B., 1961. The thermodynamic theory of nonhydrostatically stressed solids. J. Geophys.
799 Res. 66, 259–271.
800 King, R.F., 1952. Dissertation, Cambridge.
801 Landauer, J.K., 1958. The creep of snow under combined stress. Transactions of the society of
802 rheology II. 175-194.
803 Li, J., Jacka, T.H., Budd, W.F., 1996. Deformation rates in combined compression and shear for
804 ice which is initially isotropic and after the development of strong anisotropy. Ann. Glaciol.,
805 23, 247-252.
806 Li, Y., Baker, I. 2021. Dynamic observations of the densification of polar firn under compression
807 using a micro-computed tomograph, J. Geophys. Res., Earth Surface,126, e2021JF006290.
808 doi:org/10.1029/2021JF006290.
809 Li, Y. 2022. Critical values of the microstructural parameters at the first critical density of the
810 densification of polar firn. Cold Reg. Sci. Technol., 198(2022), 10355.
811 doi:org/10.1016/j.coldregions.2022.103553.
812 Li, Y., Baker, I. 2022a. Observations of the creep of polar firn. J. Glaciol., 68(268), 269–287.
813 doi.org/10.1017/jog.2021.91.

814 Li, Y., Baker, I. 2022b. Metamorphism observation and model of snow from Summit, Greenland
815 under both positive and negative temperature gradients in a Micro CT, Hydrol. Processes,
816 e14696. doi.10.1002/HYP.14696.
817 Li, Y. 2023a. Are bubbles in ice the potential space for hydrogen storage? Int. J. Hydrogen
818 Energy, 50(D), 575-585. doi.org/10.1016/j.ijhydene.2023.07.273.
819 Li, Y. 2023b. Changes in grain size during the relaxation stage of viscoelastic firn, Philos. Mag.,
820 104(4), 239-259. doi.org/10.1080/14786435.2023.2296656.
821 Li, Y. Fu, C. Keegan, C. et al. 2023. Microstructural characterization of depth hoar and ice-crust
822 layers using a micro-CT, and hypothesis of ice-crust formation under a thunderstorm, Hydrol.
823 Processes, 37(12), e15060. doi.org/10.1002/hyp.15060.
824 Li, Y. 2024a. Hydrogen production via imperfective ice I*h*. Int. J. Hydrogen Energy. 100, 727–
825 735.
826 Li, Y. 2024b. Hydrogen storage-learn from the air clathrate hydrate in polar ice sheets.
827 Sustainable Energy Technol. Assess. 72, 104007.
828 Li, Y. 2024c. The improvement of hydrogen storage capacity via bubbles nucleated in ice-like
829 nanotubes, Mater. Today Sustainability, 27, 100856.
830 Liu, K., Sun, R. & Daraio, C. 2022. Growth rules for irregular architected materials with
831 programmable properties. Sci., 377(6609), 975-981.
832 Lundin, J.M., Stevens, C.M., Arthern, R., Buizert, C., Orsi, A., Ligtenberg, S.R., et al. 2017. Firn
833 model intercomparison experiment (FirnMICE). J. Glaciol. 63(239), 401–422.
834 https://doi.org/10.1017/jog.2016.114.
835 Maeno, N., Ebinuma, T., 1983. Pressure sintering of ice and its implication to the densification of
836 snow at polar glaciers and ice sheets. J. Phys. Chem. 87, 4103–4110.
837 Mellor, M., Smith, J.H., 1966. Creep of snow and ice, CRREL Res. Rep. 220.
838 Mellor, M., Testa, R., 1969. Effect of temperature on the creep of ice. J. Glaciol., 8(52), 131-145.

839 Mellor, M., 1975. A review of basic snow mechanics. Int. Assoc. Hydrol. Sci. 114, 251–291.
840 Meussen, B., Mahrenholtz, O., Oerter, H., 1999. Creep of polar firn. Cold Reg. Sci. Technol. 29,
841 177–200. doi: 10.1016/S0165-232X(99)00018-X
842 Nasello, O.B., Di Prinzio, C.L., Guzman, P.G., 2005. Temperature dependence of "pure" ice grain
843 boundary mobility, Acta Mater., 53(18) 4863-4869, doi: 10.1016/j.actamat.2005.06.022.
844 Ogunmolasuyi, A., Murdza, A., Baker, I. 2023. The onset of recrystallization in polar firn.
845 Geophys. Res. Lett., 50, e2023GL103435. doi.org/10.1029/2023GL103435.
846 Paterson, W.S.B., 1977. Secondary and tertiary creep of glacier ice as measured by borehole
847 closure rates, Rev. Geophys. Space Phys., 15, 47–55.
848 Perutz, M.F., Seligman, G., 1939. A crystallographic investigation of glacier structure and the
849 mechanism of glacier flow. Proc. Roy. Soc. London A 172, 335–360.
850 Petrenko, V.F., Whitworth, R.W., 1999. Physics of Ice. Oxford: Oxford University Press.
851 Pimienta, P., Duval, P., 1987. Rate controlling processes in the creep of polar glacier ice. Journal
852 de Physique, 48, 243-248.
853 Raymond, C.F., 1973. Inversion of flow measurements for stress and rheological parameters inva
854 valley glacier. J. Glaciol. 12, 19–44.
855 Salamatin, A.N., Lipenkov, V.Y., Barnola, J.M., Hori, A., Duval, P., Hondoh, T. 2009. Snow/firn
856 densification in polar ice sheets. In: Hondoh, T. (Ed.), III. Firn densification, close-off and
857 chronology, 195-222, Hokkaido University Press.
858 Salm, B., 1982. Mechanical properties of snow. Rev. Geophys. Space Phys., 20(N1), 1–19.
859 Scapozza, C., Bartelt, P.A., 2003. The influence of temperature on the small-strain viscous
860 deformation mechanics of snow: a comparison with polycrystalline ice. Ann. Glaciol., 37,
861 90–96.

862 Schleef, S., Lowe, H., Schneebeli, M., 2014. Influence of stress, temperature and crystal
863 morphology on isothermal densification and specific surface area decrease of new snow. T.
864 Cryosphy., 8, 1825-1838.
865 Sinha, N.K., 1978. Short-term rheology of polycrystalline ice. J. Glaciol., 21(85) 457-472.
866 Steinemann, S., 1954. Flow and recrystallisation of ice. Proc. Int. Assoc. Hydrol. Sci. 39, 449–
867 462.
868 Song, M., Baker, I., Cole, D.M., 2005. The effect of particles on dynamic recrystallization and
869 fabric development of granular ice during creep. J. Glaciol. 51(173), 377–382. doi:
870 10.3189/172756505781829287.
871 Song, M., Cole, D.M., Baker, I., 2006a. Investigation of Newtonian creep in polycrystalline ice.
872 Philos. Mag. Lett. 86(12), 763–771. doi: 10.1080/09500830601023787.
873 Song, M., Cole, D.M., Baker, I. 2006b. An investigation of the effects of particles on creep of
874 polycrystalline ice. Scr. Mater. 55, 91–94. doi: 10.1016/j.scriptamat.2006.03.029.
875 Song, M., Baker, I., Cole, D.M., 2008. The effect of particles on creep rate and microstructures of
876 granular ice. J. Glaciol. 54(186), 533–537. doi: doi:10.3189/002214308785836959.
877 Theile, T., Lowe, H., Theile, T.C., Schneebeli, M., 2011. Simulating creep of snow based on
878 microstructure and the anisotropic deformation of ice. Acta Mater. 59, 7104–7113. doi:
879 10.1016/j.actamat.2011.07.065.
880 Thomas, R.H., MacAyeal, D.R., Bentley, C.R., Clapp, J.L., 1980. The creep of ice, geothermal
881 heat flow, and Roosevelt Island, Antarctica. J. Glaciol. 25, 47–60.
882 Treverrow, A., Budd, W.F., Jacka, T.H., Warner, R.C., 2012. The tertiary creep of polycrystalline
883 ice: experimental evidence for stress-dependent levels of strain-rate enhancement. J. Glaciol.
884 58(208), 301–314. doi: 10.3189/2012JoG11J149.
885 Vickers, W., Greenfield, P., 1968. The high temperature creep properties of compacted
886 magnesium powder. *Journal of Nuclear Materials,* 27(1), 73-79.

887 Wang, X., Baker, I., 2013. Observation of the Microstructural Evolution of Snow under Uniaxial
888 Compression using X-ray Computed Micro-tomography, J. Geophys. Res., 118, 1-12,
889 doi.org/10.1002/2013JD020352.
890 Weertman, J., 1983. Creep deformation of ice. Annual Review Earth Planet Science, 11, 215–240.
891 Weertman, J., 1985. Unsolved problems of creep. Nat. 314(6008), 227.
892 Wiese, M., Schneebeli, M., 2017. Snowbreeder 5: a Micro-CT device for measuring the
893 snow-microstructure evolution under the simultaneous influence of a temperature gradient
894 and compaction. J. Glaciol., 63(238), 355–360, doi: 10.1017/jog.2016.143.